Nano Research
2023, 16(5): 7777–7783

ISSN 1998-0124 CN 11-5974/O4
https://doi.org/10.1007/s12274-023-5430-z

Research Article

Synergetic effects of gold-doped copper nanowires with low Au content for enhanced electrocatalytic CO_2 reduction to multicarbon products

Zongnan Wei[1,2], Shuai Yue[1,2], Shuiying Gao[2,3], Minna Cao[2,3] (✉), and Rong Cao[2,3,4] (✉)

[1] *Department of Chemistry, University of Science and Technology of China, Hefei 230026, China*
[2] *State Key Laboratory of Structural Chemistry, Fujian Institute of Research on the Structure of Matter, Chinese Academy of Sciences, Fuzhou 350002, China*
[3] *University of Chinese Academy of Sciences, Beijing 100049, China*
[4] *Fujian Science & Technology Innovation Laboratory for Optoelectronic Information of China, Fuzhou 350108, China*

Received: 17 October 2022 / **Revised:** 6 December 2022 / **Accepted:** 21 December 2022

ABSTRACT

As efficient catalysts of electrochemical CO_2 reduction reaction (CO_2RR) towards multicarbon (C_{2+}) products, Cu-based catalysts have faced the challenges of increasing the reactive activity and selectivity. Herein, we decorated the surface of Cu nanowires (Cu NWs) with a small amount of Au nanoparticles (Au NPs) by the homo-nucleation method. When the Au to Cu mass ratio is as little as 0.7 to 99.3, the gold-doped copper nanowires (Cu-Au NWs) could effectively improve the selectivity and activity of CO_2RR to C_{2+} resultants, with the Faradaic efficiency (FE) from 39.7% (Cu NWs) to 65.3%, and the partial current density from 7.0 (Cu NWs) to 12.1 mA/cm^2 under −1.25 V vs. reversible hydrogen electrode (RHE). The enhanced electrocatalytic performance could be attributed to the following three synergetic factors. The addition of Au nanoparticles caused a rougher surface of the catalyst, which allowed for more active sites exposed. Besides, Au sites generated *CO intermediates spilling over into Cu sites with the calculated efficiency of 87.2%, which are necessary for multicarbon production. Meanwhile, the interphase electron transferred from Cu to Au induced the electron-deficient Cu, which favored the adsorption of *CO to further generate multicarbon productions. Our results uncovered the morphology, tandem, and electronic effect between Cu NWs and Au NPs facilitated the activity and selectivity of CO_2RR to multicarbons.

KEYWORDS

electrochemical CO_2 reduction, multicarbon production, bimetallic catalyst, Cu nanowires, Au nanoparticles

1 Introduction

Excessive carbon dioxide accumulation from the consumption of conventional fossil fuels has caused a series of problems like global warming and ocean acidification [1]. The electrochemical CO_2 reduction reaction (CO_2RR) serves as a promising approach to disrupt the status quo toward the carbon-neutral future [2–4], which could convert CO_2 into value-added fuels such as ethylene [5, 6], ethanol [7, 8], and n-propanol [9, 10] with the advantage of high energy density and broad applications. Although CO_2RR to multicarbon (C_{2+}) products attracts enormous attention, it has been confronted with sluggish thermodynamics and kinetics. On the one hand, linear CO_2 molecules are chemical inert by virtue of the significantly high bonding energy of C=O (750 kJ/mol), making CO_2 hard to be converted into other chemicals containing C–C (336 kJ/mol), C–O (327 kJ/mol), and C–H (411 kJ/mol) bonds. On the other hand, the generation of multicarbons involves multiple electron–proton transfer and C–C coupling, which have to overcome the high energy barrier and high overpotentials [11]. Except for the own difficulty of CO_2RR, hydrogen evolution reaction (HER) as the competitive reaction occurs unavoidably due to the low solubility for CO_2, causing the mass transfer limitation in liquid electrolyte. Hence, highly active electrocatalysts are urgently needed to address the bottleneck of the CO_2RR to multicarbons.

Among a wide variety of metals, Cu-based catalysts stand out with the uniqueness of both the negative adsorption energy for *CO and positive adsorption energy for *H [12], recognized as the most effective catalysts for CO_2RR to multicarbons. However, Cu electrocatalysts are plagued by problems of insufficient activity and selectivity for CO_2RR for the reason of chemically inert CO_2 reactants and the similar equilibrium potentials for reducing to different products. To date, several strategies have been engineered to address these issues. For example, one of the efficacious approaches is based on the morphological effect [13–16], since the crystal defects and facets are known to directly influence the CO_2RR. Gao et al. confirmed that cubooctahedron-shaped Cu favored the production of multicarbons compared with the various shaped Cu catalysts [17]. The enhancement was attributed to Cu (100)/Cu (111) interfaces, which provided a favorable local electronic structure to encourage the rate-limiting C–C coupling step. Among those, Cu nanowires (Cu NWs) feature a high aspect ratio and rich grain boundaries with five-fold twinned structures,

Address correspondence to Rong Cao, rcao@fjirsm.ac.cn; Minna Cao, mncao@fjirsm.ac.cn

which are confirmed to facilitate electron transport and offer abundant active sites for CO_2RR [18, 19].

Another remarkable strategy is introducing a secondary metal [20], such as Au [21, 22], Ag [23, 24], and Pd [25], which can boost the surface coverage of *CO, the necessary intermediate in all pathways of producing multicarbons [26]. Buonsanti et al. developed Ag-Cu nanodimers with an enhanced selectivity of ethylene via the tandem and electronic effects [27]. Compared with Ag, Au presents superior chemical stability and selectively for CO_2 reduction to CO [28, 29] and a larger work function [30], so Au has the potential as a second metal for Cu-based catalysts. Meanwhile, Sargent et al. confirmed that introducing Au in Cu catalysts could suppress HER efficiently relative to Cu [31]. However, several CuAu electrocatalysts were too easy to desorb *CO which tended to form methane or carbon monoxide instead of multicarbon products [32, 33]. For example, Wang et al. reported an elaborate Au-Cu catalyst composed of an alloyed AuCu shell and a Cu core exhibited a high CO Faradaic efficiency (FE) approaching 94% with 17% Au content [34]. Furthermore, in consideration of the rareness and high expense of Au, it is imperative to investigate how to obtain more multicarbon products by the optimal synergetic effects between Cu and Au at a considerable Au utilization efficiency.

In this context, we reported an advanced CO_2RR catalyst by doping a small number of gold nanoparticles (Au NPs) onto the surface of Cu NWs via homo-nucleation of the Au(0) species at different Au/Cu ratios. Specifically, $Cu_{99.3}Au_{0.7}$ nanowires ($Cu_{99.3}Au_{0.7}$ NWs) exhibited even considerably higher Faradaic efficiency of multicarbon products approaching 65.3% than pure Cu NWs (39.7%) but at a low Au content of 0.7%. Concomitantly, the partial current density increased greatly from 7.0 to 12.1 mA/cm^2. The augmentation could be owing to the surface roughness, the tandem effect, and the electronic effect. $Cu_{99.3}Au_{0.7}$ NWs enabled an ~ 87.2% efficient spillover of *CO intermediates from Au sites, which were further reduced by the electron-deficient Cu sites generated from the charge transfer from Cu to Au. On contrary, limited active Cu sites on Cu NWs favored such competitive productions as hydrogen and formate with lower energy barriers. This work brings a deeper understanding of both the structures and interactions between the various metals for the CO_2RR catalyst to facilitate breaking through the existing barrier of selectivity and activity.

2 Results and discussion

Cu-Au NWs were synthesized by the deposition of Au NPs on Cu NWs (Fig. 1) [35]. Firstly, the Cu NWs were prepared according to the reported literature with small modifications [36]. Subsequently, the $HAuCl_4$ solution was rapidly introduced into the Cu NWs solution with the presence of ascorbic acid (AA). The gold precursor was instantaneously reduced, leading to a rapidly increased concentration of Au(0) species around Cu NWs, followed by further initiated nucleation and crystal growth on their own. The catalysts of different Cu to Au mass ratios were obtained by changing the amounts of $HAuCl_4$ solution, denoted as $Cu_{99.8}Au_{0.2}$, $Cu_{99.3}Au_{0.7}$, and $Cu_{96.7}Au_{3.3}$ NWs.

The morphology and size of $Cu_{99.3}Au_{0.7}$ NWs as the representative were characterized by scanning electron microscopy (SEM) and transmission electron microscopy (TEM) (Fig. 1). The Cu NWs possessed a linear morphology with a flat and clean surface (Fig. S1 in the Electronic Supplementary Material (ESM)). A band-like contrast on the NWs was induced by bending or twisting [37]. After surface modification of Au NPs, the nanowires showed a uniformly linear morphology consistent with Cu NWs (Fig. 2(a)). As shown in Figs. 2(b) and 2(c), the Au nanoparticles

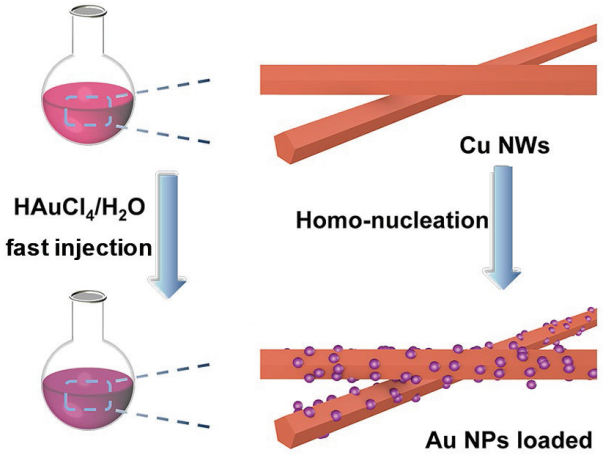

Figure 1 Schematic illustration of the preparation of Cu-Au NWs by decorating Au NPs on the surfaces via the homo-nucleation of Au(0) species.

were loaded on the surface of Cu NWs with an average size of 5.9 ± 0.6 nm. High-resolution transmission electron microscopy (HRTEM) images of both Cu-Au and Cu NWs showed the exposed lattice spacings of 0.21, 0.18, and 0.13 nm, respectively, which can be assigned to the (200), (111), and (220) plane of Cu. Cu-Au NWs distinguished the lattice spacing of 0.24 nm for the bulging particles, which can be assigned to Au (111) plane (Fig. 1(d)). The elemental mapping using energy dispersive X-ray spectroscopy (EDS) indicated the spatial distributions of Cu and Au (Figs. 2(f)–2(g)). According to the mapping data, the Cu signals were distributed in the core, while the small spheres composed of Au were evenly distributed across, confirming the formation of Au NPs loaded on the surface of Cu NWs. Furthermore, as shown in Figs. S3–S5 in the ESM, the more content of Au, the more Au NPs distributed on the Cu NW surface.

Several characterizations were executed to gain insight into the composition and electronic structures of Cu and Cu-Au NWs. X-ray diffraction (XRD) data confirmed the Cu crystal structures of all samples (Fig. 3(a)). There were two peaks at 2θ = 43.3° and 50.4°, corresponding to the diffractions in the (111) and (200) of the face-centered cubic (fcc) Cu (JCPDS 04-0836), which suggested the fcc structure typical of Cu in the Cu and Cu-Au NWs. It is noteworthy that there was no Bragg angle shift for the Cu diffraction signal, indicating a phase-separated bimetallic nature of the Cu-Au NWs without the CuAu alloy. In the ultraviolet–visible (UV–vis) extinction spectra, primarily localized surface plasmon resonance (LSPR) peaks were also associated with Cu (Fig. 3(b)). As the Au content increased, the peak exhibited a red shift from 568 to 580 nm, indicating the charge transfer between Cu NWs and Au dopants. Due to the relatively small amounts of Au, no obvious Au-related peaks were found in both the XRD patterns and the UV–vis extinction figures while the loading of Au could be confirmed by X-ray photoelectron spectroscopy (XPS) and inductively coupled plasma optical emission spectroscopy (ICP-OES). By integration of corresponding XPS peaks, the surface of $Cu_{99.3}Au_{0.7}$ contained 96.1% of Cu and 3.9% of Au, while the bulk was measured to be 99.3% of Cu and 0.7% of Au obtained by ICP-OES (Table S1 in the ESM). This difference also occurred in the other two samples, as confirmed that Au dopants were mainly distributed on the sample surface.

Furthermore, the electronic interaction between Cu and Au was also verified in the high-resolution XPS spectra (Figs. 3(c) and 3(d)). The peak of Cu $2p_{3/2}$ shifted from 932.2 (Cu NWs) to 932.5 eV ($Cu_{99.3}Au_{0.7}$ NWs) and further to 932.7 eV for $Cu_{96.7}Au_{3.3}$ NWs corresponding to the binding energy of Cu $2p_{1/2}$ from 952.1

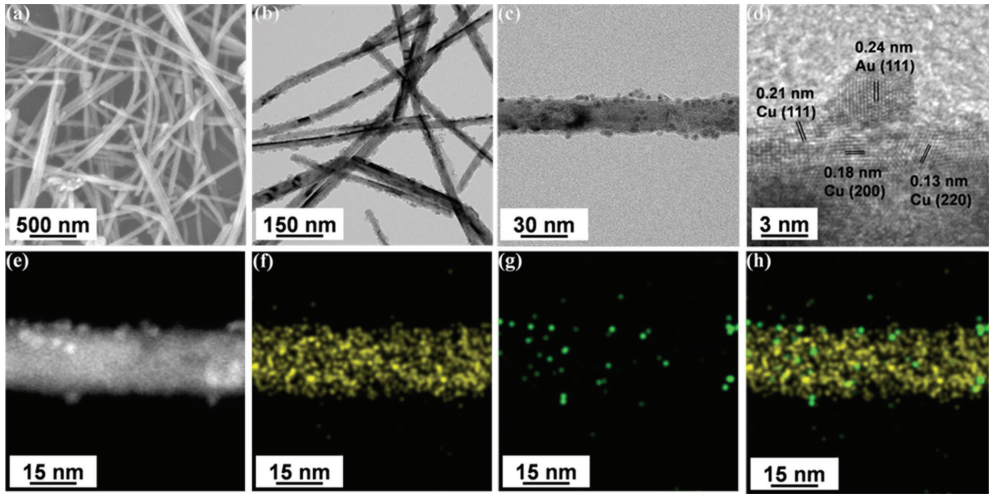

Figure 2 (a) SEM, (b) low-, (c) high-magnification TEM, (d) HRTEM, (e) high-angle annular dark-field scanning transmission electron microscopy (HAADF-STEM) images, and (f)–(h) the corresponding EDS mapping images of Cu-Au NWs. In the EDS elemental mapping, yellow color represents Cu, and green color represents Au.

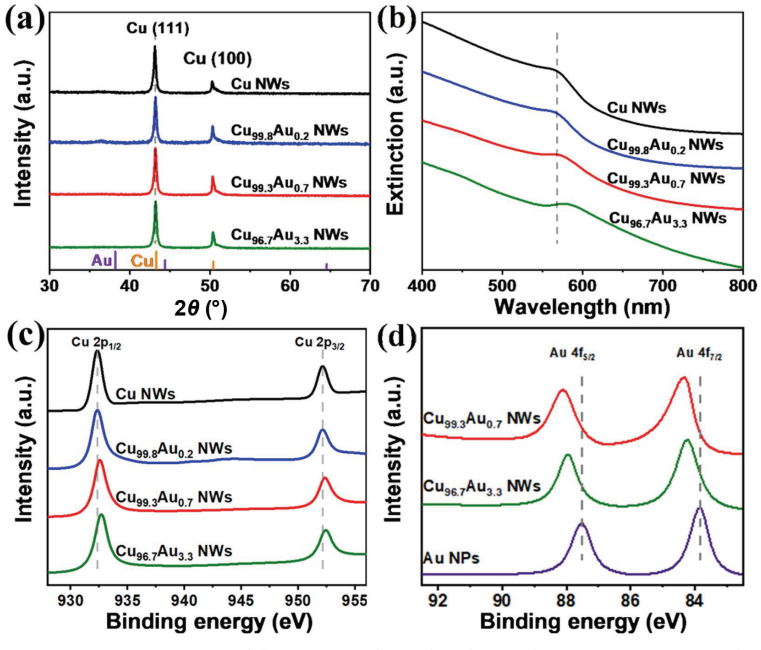

Figure 3 (a) XRD patterns and (b) UV–vis extinction spectra of the as-prepared samples of Cu and Cu-Au NWs, respectively. High-resolution XPS spectra of (c) Cu 2p from the Cu-Au and Cu NWs and (d) Au 4f from the Cu-Au NWs and Au NPs.

to 952.5 eV. To get sight into the electronic state of gold, similar spherical Au NPs were obtained with an average size of 6.6 nm (Fig. S6 in the ESM). For the Au counterpart, the shift of the binding energy of Au $4f_{7/2}$ presented the opposite trend from 84.3 ($Cu_{99.3}Au_{0.7}$ NWs) to 83.8 eV (Au NPs). The Au atomic fraction of the $Cu_{99.8}Au_{0.2}$ sample could not achieve the lowest detection limit of XPS test, so the discussion of Au 4f peak shift was conducted on the other samples. These changes of binding energy positions could be explained by the interphase electron transfer from Cu to Au atoms. As the electron donor, the energy binding of Cu increased, while that of Au as the electron acceptor decreased.

Inspired by the above characterizations, the linear morphology and the electron transfer of Cu-Au NWs provided the potential for the CO_2RR to multicarbon products. The electrocatalytic CO_2RR performances of Cu-Au NWs were tested in an H-type three-electrode cell in CO_2-saturated mixed 0.1 M $KHCO_3$ and 0.1 M KCl (Fig. 4) along with Cu NWs and Au NPs as comparisons. The CO_2RR product distribution was obtained using gas chromatographic (GC) analysis for gas products and nuclear magnetic resonance (NMR) analysis for liquid products via the internal standard method. The linear sweep voltammetry (LSV) curves of all samples were conducted at a sweeping rate of 10 mV/s (Fig. 4(a)). As noted by the total current densities at potentials in the range of 0 to 1.5 V vs. reversible hydrogen electrode (RHE), the Cu-Au nanowires showed a clearly rapid increment, wherein $Cu_{99.3}Au_{0.7}$ NWs obtained the largest current density. This observation suggested that the moderate amount of Au NPs doped could contribute to the enhanced CO_2RR activity of the nanowires.

The selectivity and partial current density for each CO_2RR product obtained were then measured and compared. As the product distribution shown in Fig. 4(b), $Cu_{99.3}Au_{0.7}$ NWs exhibited excellent selectivity for the multicarbon products. For $Cu_{99.3}Au_{0.7}$ NWs, FEs of total C_{2+} products were boosted from 39.7% for pristine Cu NWs to 65.3%, while the C_1 and H_2 productions were inhibited from 27.3% and 30.1% to less than 15% and 19% at −1.25 V vs. RHE. The major C_{2+} products were ethylene (35.0%) and ethanol (19.1%) with small amounts of n-propanol (8.0%) and acetate (3.3%). When the applied potentials extended to the range of −1.1 and −1.4 V vs. RHE, the FEs of the multicarbon

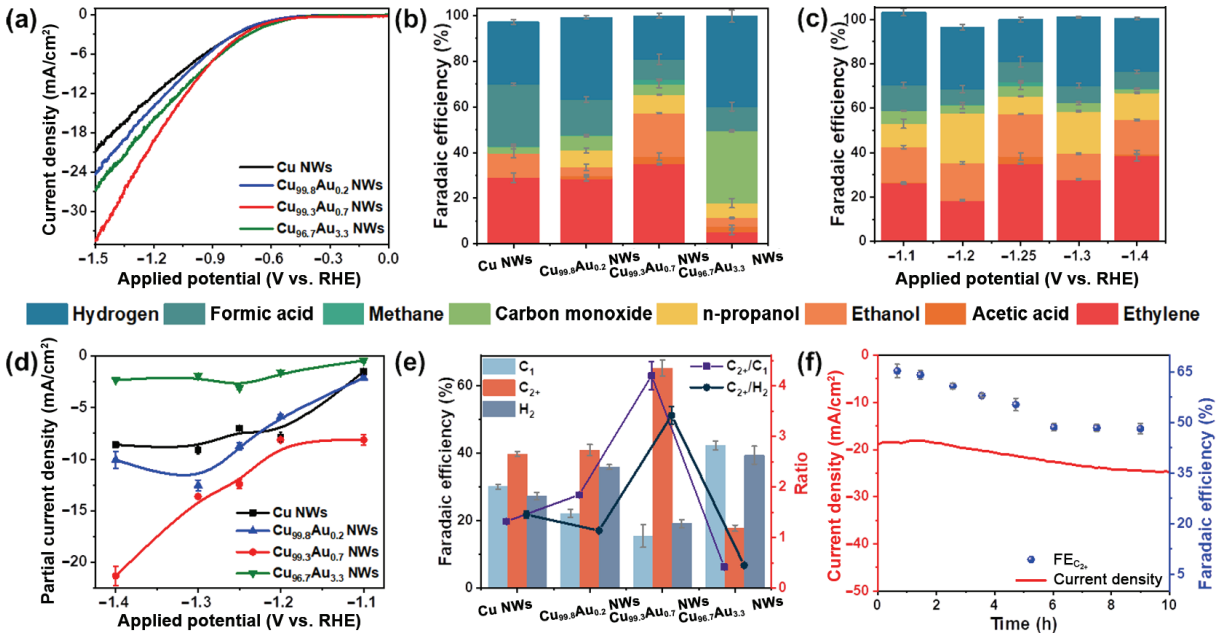

Figure 4 (a) LSV curves with the Cu and Cu-Au NWs, respectively. (b) The selectivity of CO_2RR at −1.25 V vs. RHE for different catalysts. (c) Total product FEs of $Cu_{99.3}Au_{0.7}$ NWs at different potentials. (d) Partial current density for the C_{2+} products over the different catalysts in 0.1 M $KHCO_3$ + 0.1 M KCl. The current densities were normalized to the geometric area. (e) FEs of H_2, C_1, and C_{2+} for the Cu and Cu-Au NWs at −1.25 V vs. RHE. (f) Electrochemical stability test of $Cu_{99.3}Au_{0.7}$ NWs under −1.25 V vs. RHE.

products for $Cu_{99.3}Au_{0.7}$ NWs could be maintained at over 53% (Fig. 4(c)). Notably, the high selectivity toward n-propanol reached 22.5% at −1.20 V vs. RHE. To explore the effect of Au content on CO_2RR performance, we also prepared $Cu_{99.5}Au_{0.5}$ and $Cu_{98.3}Au_{1.7}$ NWs for comparison (Fig. S9 in the ESM). For $Cu_{99.8}Au_{0.2}$ NWs, the highest FEs of C_{2+} products were below 55.0% and the H_2 FEs were maintained at ~ 34% at −1.3 V vs. RHE. The selectivity of $Cu_{99.5}Au_{0.5}$ NWs was maintained at 55% within a wide potential range. When the Au mass ratio was 0.7%, the selectivity reached the highest value with the 65.3 % FE of C_{2+} products. When the Au content further increased, $Cu_{96.7}Au_{1.7}$ and $Cu_{98.3}Au_{3.3}$ NWs exhibited poor selectivity of C_{2+} productions as the $FE_{C_{2+}}$ was below 30% at all applied potentials. Carbon monoxide, formic acid, and hydrogen are the main products of $Cu_{96.7}Au_{1.7}$ and $Cu_{98.3}Au_{3.3}$ NWs. Correspondingly, Au NPs favored the selectivity of carbon monoxide at low potential. As the potential became more negative, the FE_{CO} decreased while the FE_{H_2} increased with a small amount of formic acid production at −1.4 V. Detailed FE data for the catalysts are displayed in Fig. S10 and Table S2 in the ESM. Accordingly, the multicarbon partial current density of $Cu_{99.3}Au_{0.7}$ NWs was up to 12.40 mA/cm² at −1.25 V vs. RHE and further increased at the more negative potential (Fig. 4(d)). In contrast, the partial current densities for Cu and $Cu_{96.3}Au_{3.3}$ NWs were less than 10 mA/cm² at the same reduction condition and the largest partial current density was 12.7 mA/cm² at −1.3 V for $Cu_{96.3}Au_{3.3}$ NWs. Thus, $Cu_{99.3}Au_{0.7}$ NWs exhibited the highest multicarbon production rate. To evaluate the selectivity towards C_{2+} versus C_1 products in CO_2RR, we compared the ratio of $FE_{C_{2+}}$ to FE_{C_1} on different catalysts at −1.25 V vs. RHE (Fig. 4(e)). Relative to the Cu NWs, the ratio of $FE_{C_{2+}}$ to FE_{C_1} for $Cu_{99.3}Au_{0.7}$ NWs was increased from 1.3 to 4.2, representing a 3.3 times improvement, further indicating the doping of Au NPs notably suppressed the C_1 production as well as promoting the generation of multicarbon. However, when more Au content was added, i.e., $Cu_{96.3}Au_{3.3}$, the decline of the $FE_{C_{2+}}$ and the FE_{CO_2RR} corresponded to a steep downward of the $FE_{C_{2+}}/FE_{H_2}$ and $FE_{C_{2+}}/FE_{C_1}$ values, which was ascribed to Au occupying the active sites of Cu on the surface. Au atoms promoted the desorption of intermediate *CO and in turn inhibited C–C coupling. As a result, the C_{2+} FEs exhibited a volcano-shaped dependence on Au nanoparticle capacity with the $Cu_{99.3}Au_{0.7}$ NWs possessing the highest C_{2+} selectivity.

With the above superior activity and selectivity, $Cu_{99.3}Au_{0.7}$ NWs could be regarded as an efficient catalyst for CO_2RR to generate multicarbons. Except for the enhanced activity and selectivity, the high stability for $Cu_{99.3}Au_{0.7}$ NWs was also confirmed under the CO_2RR electrolysis of −1.25 V vs. RHE for 10 h. After 10 h, the $FE_{C_{2+}}$ maintained ~ 50%, corresponding to ~ 75% retention. The TEM and HRTEM images confirmed the preservation of the one-dimensional (1D) morphology of $Cu_{99.3}Au_{0.7}$ NWs (Fig. S10 in the ESM). The XPS spectra presented similar spectra before and after the CO_2RR test (Fig. S11 in the ESM). Hence, the morphology and the electronic structures of the post-reaction $Cu_{99.3}Au_{0.7}$ NWs have been stably preserved.

To gain an ideal CuM (M represents an additional metal) linear catalyst, it is important to get insight into the enhanced selectivity and activity of $Cu_{99.3}Au_{0.7}$ NWs. A schematic description showing the proposed mechanism behind the electrocatalytic enhancement of the Cu-Au NWs is plotted in Fig. 5(a). Firstly, the electrochemical surface area (ECSA) for various nanowires was analyzed by the double-layer capacitance test after the Au nanoparticles modification (Fig. S12 in the ESM). The largest ECSA was obtained on the $Cu_{99.3}Au_{0.7}$ NWs with 1.6 times larger than that of Cu NWs, in conjunction with the highest current density [38]. Although $Cu_{99.3}Au_{0.7}$ and $Cu_{96.3}Au_{3.3}$ NWs had similar ECSA, their catalytic performances for the reduction favor of multicarbon and carbon monoxide were not nearly identical, suggesting the higher surface area was not the only reason for the augmented CO_2RR.

Secondly, as the tandem effect was also widely applied in bimetallic catalytic systems [39–41], we researched the roles of Cu and Au in the process of CO_2RR. The tandem process of CO_2RR to multicarbon products involved the CO_2RR to *CO, the *CO overspill into the neighbor metal, and the coupling of two *CO. Our result verified that Au was an excellent CO_2RR to CO catalyst (Fig. S6(d) in the ESM). In our system, the CO production rates on $Cu_{99.3}Au_{0.7}$ NWs were much higher than Cu NWs, increasing with more negative potential while the production rate of gaseous CO was maintained at ~ 2 μmol/s (Fig. S13 in the ESM).

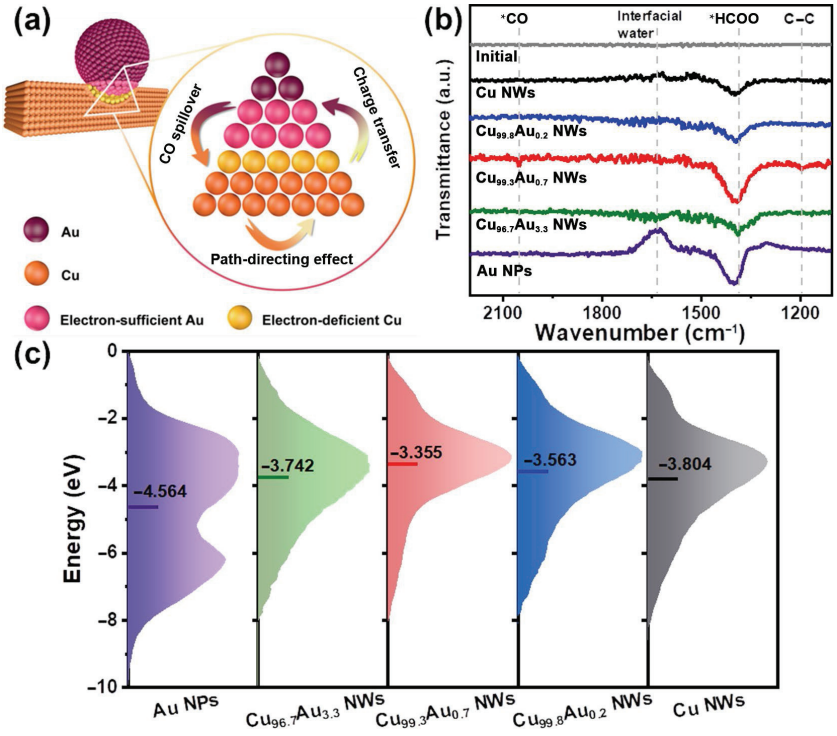

Figure 5 (a) Schematic representation of the proposed mechanism of C_{2+} promotion in the Cu-Au NWs, which couples the path-directing effect of the high aspect ratio nanowire morphology, the tandem catalysis induced by Au and Cu as separated phases, and the electronic effect caused by the charge transfer at the interface. (b) *In situ* electrochemical ATR-FTIR spectra of Cu NWs, Cu-Au NWs, and Au NPs at −1.25 V vs. RHE in the CO_2-saturated mixture of 0.1 M KCl and 0.1 M $KHCO_3$ at the firth minute. (c) Surface valence band photoemission spectra of Cu NWs, Cu-Au NWs, and Au NPs.

Furthermore, normalized by the ECSA, the CO spillover efficiency at −1.25 V vs. RHE was 87.2%, indicating that ~ 87% of the CO was produced on Au sites [42]. Furthermore, *in situ* electrochemical attenuated total reflection Fourier transformed infrared (ATR-FTIR) spectroscopy was employed for the reaction intermediate (Fig. 5(b)). All three samples exhibited the infrared peak at around 1400 cm^{-1} which was associated with *HCOO [43, 44]. Compared with those of the Cu NWs and Au NPs, the red shift of 10 cm^{-1} was observed for the *HCOO band on the $Cu_{99.3}Au_{0.7}$ NWs, suggesting the enhanced adsorption strength of *HCOO. Compared with Cu NWs and Au NPs, two new peaks were observed at 1195 and 2050 cm^{-1} on the $Cu_{99.3}Au_{0.7}$ NWs, which were related with the C–C vibration band and *CO. These peaks disclosed that the $Cu_{99.3}Au_{0.7}$ NWs showed a strong interaction with the *CO and following C–C coupling. To further evaluate the interaction between the intermediates and catalyst surface, surface valence band photoemission spectra of Cu NWs, Cu-Au NWs, and Au NPs were collected (Fig. 5(c)). Among them, Au NPs had the lowest lying d-band center, suggesting the weakest binding ability with CO. This result could elucidate that Au NPs exhibited a high selectivity of CO, which would be an essential prerequisite for the tandem effect. By contrary, $Cu_{99.3}Au_{0.7}$ NWs had the highest lying d-band center, indicating the enhanced adsorption strength of *CO intermediates [45, 46], which was consistent with the result of *in situ* ATR-FTIR.

Lastly, as demonstrated by XPS and UV–vis spectra, it can be inferred that the formation of electron-deficient Cu sites generated from the interphase electron transfer from Cu to Au atoms would favor the adsorption of *CO intermediates. Above all, the $Cu_{99.3}Au_{0.7}$ NWs exhibited the remarkable performance compared with the other materials reported in the previous literature (Table S3 in the ESM). The CO_2RR improvement of $Cu_{99.3}Au_{0.7}$ NWs could be attributed to the enhanced adsorption of the intermediates and the promoted C–C coupling, favoring the multicarbon productions.

3 Conclusions

In summary, built on the superior structural condition of nanowires, we have developed Cu-Au NWs loaded Au NPs on the Cu nanowire surface through Au(0) homo-nucleation strategy. Among those, $Cu_{99.3}Au_{0.7}$ NWs led to the optimal selectivity and activity of C_{2+} products. The introduction of Au nanoparticles on the Cu NW could bring more active sites, the CO spillover, and the electron transfer between Cu and Au. The *in situ* ATR-FTIR results together with surface valence band photoemission spectra demonstrated that $Cu_{99.3}Au_{0.7}$ NWs had the strongest interaction between the catalyst surface and the *CO intermediate and the following step of *CO dimerization for the multicarbon products. Our work suggested an effective Cu-based catalyst for CO_2 electrochemical reduction and highlighted the critical role of intermetallic interactions in the design of bimetallic catalysts.

Acknowledgements

We appreciate the financial support from the National Key Research and Development Program of China (Nos. 2017YFA0700103, 2018YFA0704502, and 2021YFA1501500), the National Natural Science Foundation of China (NSFC) (No. 22033008), and Fujian Science & Technology Innovation Laboratory for Optoelectronic Information of China (No. 2021ZZ103).

Electronic Supplementary Material: Supplementary material (TEM and HRTEM images; SEM images; EDS mapping spectra; XPS measurements; LSV curves; and Faradaic efficiencies of products for CO_2RR) is available in the online version of this article at https://doi.org/10.1007/s12274-023-5430-z.

References

[1] Li, Z.; Wu, R.; Zhao, L.; Li, P. B.; Wei, X. X.; Wang, J. J.; Chen, J. S.; Zhang, T. R. Metal-support interactions in designing noble metal-based catalysts for electrochemical CO_2 reduction: Recent advances and future perspectives. *Nano Res.* **2021**, *14*, 3795–3809.

[2] Cai, Z.; Zhang, Y. S.; Zhao, Y. X.; Wu, Y. S.; Xu, W. W.; Wen, X. M.; Zhong, Y.; Zhang, Y.; Liu, W.; Wang, H. L. et al. Selectivity regulation of CO_2 electroreduction through contact interface engineering on superwetting Cu nanoarray electrodes. *Nano Res.* **2019**, *12*, 345–349.

[3] Hou, Y.; Huang, Y. B.; Liang, Y. L.; Chai, G. L.; Yi, J. D.; Zhang, T.; Zang, K. T.; Luo, J.; Xu, R.; Lin, H. et al. Unraveling the reactivity and selectivity of atomically isolated metal-nitrogen sites anchored on porphyrinic triazine frameworks for electroreduction of CO_2. *CCS Chem.* **2019**, *1*, 384–395.

[4] Xia, D.; Yu, H. Y.; Xie, H.; Huang, P.; Menzel, R.; Titirici, M. M.; Chai, G. Recent progress of Bi-based electrocatalysts for electrocatalytic CO_2 reduction. *Nanoscale* **2022**, *14*, 7957–7973.

[5] Xiong, L. K.; Zhang, X.; Yuan, H.; Wang, J.; Yuan, X. Z.; Lian, Y. B.; Jin, H. D.; Sun, H.; Deng, Z.; Wang, D. et al. Breaking the linear scaling relationship by compositional and structural crafting of ternary Cu-Au/Ag nanoframes for electrocatalytic ethylene production. *Angew. Chem., Int. Ed.* **2021**, *60*, 2508–2518.

[6] Zhang, T. Y.; Bui, J. C.; Li, Z. Y.; Bell, A. T.; Weber, A. Z.; Wu, J. J. Highly selective and productive reduction of carbon dioxide to multicarbon products via *in situ* CO management using segmented tandem electrodes. *Nat. Catal.* **2022**, *5*, 202–211.

[7] Xu, H. P.; Rebollar, D.; He, H. Y.; Chong, L. N.; Liu, Y. Z.; Liu, C.; Sun, C. J.; Li, T.; Muntean, J. V.; Winans, R. E. et al. Highly selective electrocatalytic CO_2 reduction to ethanol by metallic clusters dynamically formed from atomically dispersed copper. *Nat. Energy* **2020**, *5*, 623–632.

[8] Li, Y. C.; Wang, Z. Y.; Yuan, T. G.; Nam, D. H.; Luo, M. C.; Wicks, J.; Chen, B.; Li, J.; Li, F. W.; de Arquer, F. P. G. et al. Binding site diversity promotes CO_2 electroreduction to ethanol. *J. Am. Chem. Soc.* **2019**, *141*, 8584–8591.

[9] Peng, C.; Luo, G.; Zhang, J. B.; Chen, M. H.; Wang, Z. Q.; Sham, T. K.; Zhang, L. J.; Li, Y. F.; Zheng, G. F. Double sulfur vacancies by lithium tuning enhance CO_2 electroreduction to n-propanol. *Nat. Commun.* **2021**, *12*, 1580.

[10] Wu, G. L.; Song, Y. R.; Zheng, Q.; Long, C.; Fan, T.; Yang, Z. J.; Huang, X. W.; Li, Q.; Sun, Y. L.; Zuo, L. L. et al. Selective electroreduction of CO_2 to n-propanol in two-step tandem catalytic system. *Adv. Energy Mater.* **2022**, *12*, 2202054.

[11] Tomboc, G. M.; Choi, S.; Kwon, T.; Hwang, Y. J.; Lee, K. Potential link between Cu surface and selective CO_2 electroreduction: Perspective on future electrocatalyst designs. *Adv. Mater.* **2020**, *32*, 1908398.

[12] Popović, S.; Smiljanić, M.; Jovanović, P.; Vavra, J.; Buonsanti, R.; Hodnik, N. Stability and degradation mechanisms of copper-based catalysts for electrochemical CO_2 reduction. *Angew. Chem., Int. Ed.* **2020**, *59*, 14736–14746.

[13] Chang, Y. B.; Zhang, C.; Lu, X. L.; Zhang, W.; Lu, T. B. Graphdiyene enables ultrafine Cu nanoparticles to selectively reduce CO_2 to C_{2+} products. *Nano Res.* **2022**, *15*, 195–201.

[14] Chen, Z.; Song, Y.; Zhang, Z. Y.; Cai, Y. F.; Liu, H.; Xie, W. X.; Deng, D. H. Mechanically induced Cu active sites for selective C–C coupling in CO_2 electroreduction. *J. Energy Chem.* **2022**, *74*, 198–202.

[15] Liu, D. D.; Zhang, Z. Y.; Feng, J. J.; Yu, Z.; Meng, F. N.; Xu, G. H.; Wang, J. M.; Wen, W.; Liu W. Atomic-level flatness on oxygen-free copper surface in lapping and chemical mechanical polishing. *Nanoscale Adv.* **2022**, *4*, 4263–4271.

[16] Zhang, Z. Y.; Cui, J. F.; Zhang, J. B.; Liu, D. D.; Yu, Z. J.; Guo, D. M. Environment friendly chemical mechanical polishing of copper. *Appl. Surf. Sci.* **2019**, *467–468*, 5–11.

[17] Wu, Z. Z.; Zhang, X. L.; Niu, Z. Z.; Gao, F. Y.; Yang, P. P.; Chi, L. P.; Shi, L.; Wei, W. S.; Liu, R.; Chen, Z. et al. Identification of Cu (100)/Cu (111) interfaces as superior active sites for CO dimerization during CO_2 electroreduction. *J. Am. Chem. Soc.* **2022**, *144*, 259–269.

[18] Chang, C. J.; Lin, S. C.; Chen, H. C.; Wang, J. L.; Zheng, K. J.; Zhu, Y. P.; Chen, H. M. Dynamic reoxidation/reduction-driven atomic interdiffusion for highly selective CO_2 reduction toward methane. *J. Am. Chem. Soc.* **2020**, *142*, 12119–12132.

[19] Zhang, L. G.; Li, N.; Gao, F. M.; Hou, L.; Xu, Z. M. Insulin amyloid fibrils: An excellent platform for controlled synthesis of ultrathin superlong platinum nanowires with high electrocatalytic activity. *J. Am. Chem. Soc.* **2012**, *134*, 11326–11329.

[20] Zhu, Y. T.; Cui, X. Y.; Liu, H. L.; Guo, Z. G.; Dang, Y. F.; Fan, Z. X.; Zhang, Z. C.; Hu, W. P. Tandem catalysis in electrochemical CO_2 reduction reaction. *Nano Res.* **2021**, *14*, 4471–4486.

[21] Fu, J. J.; Zhu, W. L.; Chen, Y.; Yin, Z. Y.; Li, Y. Y.; Liu, J.; Zhang, H. Y.; Zhu, J. J.; Sun, S. H. Bipyridine-assisted assembly of Au nanoparticles on Cu nanowires to enhance the electrochemical reduction of CO_2. *Angew. Chem., Int. Ed.* **2019**, *58*, 14100–14103.

[22] Morales-Guio, C. G.; Cave, E. R.; Nitopi, S. A.; Feaster, J. T.; Wang, L.; Kuhl, K. P.; Jackson, A.; Johnson, N. C.; Abram, D. N.; Hatsukade, T. et al. Improved CO_2 reduction activity towards C_{2+} alcohols on a tandem gold on copper electrocatalyst. *Nat. Catal.* **2018**, *1*, 764–771.

[23] Choi, C.; Cai, J.; Lee, C.; Lee, H. M.; Xu, M. J.; Huang, Y. Intimate atomic Cu-Ag interfaces for high CO_2RR selectivity towards CH_4 at low over potential. *Nano Res.* **2021**, *14*, 3497–3501.

[24] Zhong, Y. Z.; Kong, X. D.; Song, Z. M.; Liu, Y.; Peng, L. P.; Zhang, L.; Luo, X.; Zeng, J.; Geng, Z. G. Adjusting local CO confinement in porous-shell Ag@Cu catalysts for enhancing C–C coupling toward CO_2 eletroreduction. *Nano Lett.* **2022**, *22*, 2554–2560.

[25] Lv, H.; Lv, F.; Qin, H. Y.; Min, X. W.; Sun, L. Z.; Han, N.; Xu, D. D.; Li, Y. G.; Liu, B. Single-crystalline mesoporous palladium and palladium-copper nanocubes for highly efficient electrochemical CO_2 reduction. *CCS Chem.* **2022**, *4*, 1376–1385.

[26] Wang, Y. H.; Liu, J. L.; Zheng, G. F. Designing copper-based catalysts for efficient carbon dioxide electroreduction. *Adv. Mater.* **2021**, *33*, 2005798.

[27] Huang, J. F.; Mensi, M.; Oveisi, E.; Mantella, V.; Buonsanti, R. Structural sensitivities in bimetallic catalysts for electrochemical CO_2 reduction revealed by Ag-Cu nanodimers. *J. Am. Chem. Soc.* **2019**, *141*, 2490–2499.

[28] Zhu, W. L.; Zhang, Y. J.; Zhang, H. Y.; Lv, H. F.; Li, Q.; Michalsky, R.; Peterson, A. A.; Sun, S. H. Active and selective conversion of CO_2 to CO on ultrathin Au nanowires. *J. Am. Chem. Soc.* **2014**, *136*, 16132–16135.

[29] Wang, H. M.; Fu, Y. Q.; Chen, Z. N.; Zhuang, W.; Cao, M. N.; Cao, R. Tunable CO_2 enrichment on functionalized Au surface for enhanced CO_2 electroreduction. *Nano Res.*, in press, https://doi.org/10.1007/s12274-022-5159-8.

[30] Zangmeister, C. D.; Picraux, L. B.; Van Zee, R. D.; Yao, Y. X.; Tour, J. M. Energy-level alignment and work function shifts for thiol-bound monolayers of conjugated molecules self-assembled on Ag, Cu, Au, and Pt. *Chem. Phys. Lett.* **2007**, *442*, 390–393.

[31] Wang, X.; Ou, P. F.; Wicks, J.; Xie, Y.; Wang, Y.; Li, J.; Tam, J.; Ren, D.; Howe, J. Y.; Wang, Z. Y. et al. Gold-in-copper at low *CO coverage enables efficient electromethanation of CO_2. *Nat. Commun.* **2021**, *12*, 3387.

[32] Kim, D.; Resasco, J.; Yu, Y.; Asiri, A. M.; Yang, P. D. Synergistic geometric and electronic effects for electrochemical reduction of carbon dioxide using gold-copper bimetallic nanoparticles. *Nat. Commun.* **2014**, *5*, 4948.

[33] Kim, D.; Xie, C. L.; Becknell, N.; Yu, Y.; Karamad, M.; Chan, K.; Crumlin, E. J.; Nørskov, J. K.; Yang, P. D. Electrochemical activation of CO_2 through atomic ordering transformations of AuCu nanoparticles. *J. Am. Chem. Soc.* **2017**, *139*, 8329–8336.

[34] Dai, S.; Huang, T. H.; Liu, W. I.; Hsu, C. W.; Lee, S. W.; Chen, T. Y.; Wang, Y. C.; Wang, J. H.; Wang, K. W. Enhanced CO_2 electrochemical reduction performance over Cu@AuCu catalysts at high noble metal utilization efficiency. *Nano Lett.* **2021**, *21*, 9293–9300.

[35] Stewart, I. E.; Ye, S. R.; Chen, Z. F.; Flowers, P. F.; Wiley, B. J. Synthesis of Cu-Ag, Cu-Au, and Cu-Pt core–shell nanowires and their use in transparent conducting films. *Chem. Mater.* **2015**, *27*, 7788–7794.

[36] Luo, M.; Zhou, M.; Da Silva, R. R.; Tao, J.; Figueroa-Cosme, L.; Gilroy, K. D.; Peng, H. C.; He, Z. K.; Xia, Y. N. Pentatwinned Cu nanowires with ultrathin diameters below 20 nm and their use as templates for the synthesis of Au-based nanotubes. *ChemNanoMat* **2017**, *3*, 190–195.

[37] Jin, M. S.; He, G. N.; Zhang, H.; Zeng, J.; Xie, Z. X.; Xia, Y. N. Shape-controlled synthesis of copper nanocrystals in an aqueous solution with glucose as a reducing agent and hexadecylamine as a capping agent. *Angew. Chem., Int. Ed.* **2011**, *50*, 10560–10564.

[38] Zhang, W.; Huang, C. Q.; Xiao, Q.; Yu, L.; Shuai, L.; An, P. F.; Zhang, J.; Qiu, M.; Ren, Z. F.; Yu, Y. Atypical oxygen-bearing copper boosts ethylene selectivity toward electrocatalytic CO_2 reduction. *J. Am. Chem. Soc.* **2020**, *142*, 11417–11427.

[39] Chen, C. B.; Li, Y. F.; Yu, S.; Louisia, S.; Jin, J. B.; Li, M. F.; Ross, M. B.; Yang, P. D. Cu-Ag tandem catalysts for high-rate CO_2 electrolysis toward multicarbons. *Joule* **2020**, *4*, 1688–1699.

[40] Jia, H. L.; Yang, Y. Y.; Chow, T. H.; Zhang, H.; Liu, X. Y.; Wang, J. F.; Zhang, C. Y. Symmetry-broken Au-Cu heterostructures and their tandem catalysis process in electrochemical CO_2 reduction. *Adv. Funct. Mater.* **2021**, *31*, 2101255.

[41] Yang, R. O.; Duan, J. Y.; Dong, P. P.; Wen, Q. L.; Wu, M.; Liu, Y. W.; Liu, Y.; Li, H. Q.; Zhai, T. Y. *In situ* halogen-ion leaching regulates multiple sites on tandem catalysts for efficient CO_2 electroreduction to C_{2+} products. *Angew. Chem., Int. Ed.* **2022**, *61*, e202116706.

[42] Gao, J.; Zhang, H.; Guo, X. Y.; Luo, J. S.; Zakeeruddin, S. M.; Ren, D.; Grätzel, M. Selective C–C coupling in carbon dioxide electroreduction via efficient spillover of intermediates as supported by *operando* Raman spectroscopy. *J. Am. Chem. Soc.* **2019**, *141*, 18704–18714.

[43] Guo, C. Y.; Guo, Y. H.; Shi, Y. M.; Lan, X. N.; Wang, Y. T.; Yu, Y. F.; Zhang, B. Electrocatalytic reduction of CO_2 to ethanol at close to theoretical potential via engineering abundant electron-donating $Cu^{\delta+}$ species. *Angew. Chem., Int. Ed.* **2022**, *61*, e202205909.

[44] Zhu, S. Q.; Jiang, B.; Cai, W. B.; Shao, M. H. Direct observation on reaction intermediates and the role of bicarbonate anions in CO_2 electrochemical reduction reaction on Cu surfaces. *J. Am. Chem. Soc.* **2017**, *139*, 15664–15667.

[45] Ma, S. C.; Sadakiyo, M.; Heima, M.; Luo, R.; Haasch, R. T.; Gold, J. I.; Yamauchi, M.; Kenis, P. J. A. Electroreduction of carbon dioxide to hydrocarbons using bimetallic Cu-Pd catalysts with different mixing patterns. *J. Am. Chem. Soc.* **2017**, *139*, 47–50.

[46] Hammer, B.; Nørskov, J. K. Theoretical surface science and catalysis-calculations and concepts. *Adv. Catal.* **2000**, *45*, 71–129.